International Journal of Hydrogen Energy 39 (2014) 9230-9240

High glass forming ability correlated with microstructure and hydrogen storage properties of a Mg-Cu-Ag-Y glass

Á. Révész[1,*], Á. Kis-Tóth[1], L.K. Varga[2], J.L. Lábár[3], T. Spassov[4]

[1]Department of Materials Physics, Eötvös University, Budapest, H-1518, P.O.B. 32, Budapest, Hungary

[2]Research Institute for Solid state Physics and Optics, Hungarian Academy of Sciences. H-1525 Budapest, P.O.B. 49, Hungary

[3]Institute for Technical Physics and Materials Science, Research Center for Natural Sciences, Hungarian Academy of Sciences, Budapest, Hungary

[4]Department of Chemistry, University of Sofia "St. Kl. Ohridski", 1 J. Bourchier str., 1164 Sofia, Bulgaria

Abstract

Thermal characterization of an as-cast $Mg_{54}Cu_{28}Ag_7Y_{11}$ bulk metallic glass revealed that this alloy exhibits excellent glass forming ability. High-resolution X-ray diffraction study and transmission electron microscopy show that heating and isothermal annealing treatment results in the nucleation of nanocrystals of several phases. The average size of these nanocrystals (~15-20 nm) only slightly varies with prolonged annealing, only their volume fraction increases. High-pressure calorimetry experiments indicate that the as-cast fully amorphous alloy exhibits the largest enthalpy of hydrogen desorption, compared to partially

[1] Corresponding author. Tel.: +36-1-372-2823; fax: +36-1-372-2811.
E-mail address: reveszadam@ludens.elte.hu (Á. Révész)

and fully crystallized states. Since the fully crystallized alloy does not desorb hydrogen, it is assumed that hydrogen storage capacity correlates only with the crystalline volume fraction of the partially crystallized $Mg_{54}Cu_{28}Ag_7Y_{11}$ BMG and additional parameters (crystalline phase selection, crystallite size, average matrix concentration) do not play a significant role.

Keywords: H-storage; bulk metallic glass; amorphous, Mg-based; glass forming ability

1. Introduction

The wish of wide-spread application of renewable green energy is in the focus of research and industry, albeit these sources, i.e. sun, wave and wind are irregularly distributed in time and space, therefore efficient energy storage is of great importance. Due to its physical and chemical advantageous properties, hydrogen could be an ideal promising energy carrier in the next decades [1]. In order to rationalize the hydrogen economy, developing cost-effective, efficient and safe storage technologies are the main issues. The use of hydrogen can generate several times more energy per mass compared to the traditional energy carriers, yet it happens as a gas at ambient conditions. The main drawback of recent industrial application is the lack of effective storage [1].

Storing hydrogen in solid-state appears to be a method with appropriate potential storage capacity to realize the hydrogen economy [2]. Recent approaches have focused on metallic hydrides, since they possess high volumetric and gravimetric hydrogen storage performance. Among them MgH_2 is particularly considered as one of the most attractive hydrogen absorbing materials, since it exhibits outstanding storage capacity (7.6 wt.%), lightweight, low environmental impact, high abundancy and low cost [2]. To improve the storage properties, kinetics and temperature of desorption of magnesium, nano-sized Mg and Mg-based metallic compound powders have been synthesized by ball milling (BM) intensively [3-8], however, all attempts to reduce the temperature of dehydrogenation below 150 degrees have failed until now. Nevertheless, other non-equilibrium techniques, such as rapid quenching (RQ) enables the formation of highly metastable structures. As was demonstrated by Zhang et al., the cooling rate as well as the Cu/Ni ratio significantly alters the dehydrogenation behaviour of RQ crystalline Mg-Ni-Cu alloys [9-10]. It was found that the substitution of Ni by Cu yields a notable increase in the hydrogen diffusion coefficient [11]. Bendersky et al. demonstrated that Mg-Ni alloys produced by the combination of RQ and

subsequent BM posses very fast H-absorption kinetics [12]. The proper addition of rear earth (Y, La, Ce) to Mg and Mg-Ni alloys by the RQ technique facilitates even more disordered systems, i.e. partially crystalline [13-14] or monolithic amorphous alloys [15-18] with further improved storage properties.

Unfortunately, the remarkably high cooling rate that is required to achieve a fully amorphous structure by RQ, causes the limitation to small sample dimensions. Nevertheless, the past two decades have demonstrated that bulk glassy alloys of particular composition can directly be cast from the liquid state. So far, numerous classes of bulk metallic glasses (BMGs) with sample size ranging from few millimetres to couple of centimetres have been discovered [19]. Due to their high glass forming ability (GFA), the critical cooling rate to achieve a fully glassy structure can be as low as 0.1 $Kmin^{-1}$ [20]. Among BMGs, magnesium-based systems are specifically interesting because of high strength, low cost and extraordinary high GFA [21-23]. The first series of Mg-based BMG discovered in 1992 by Inoue et al. was $Mg_{90-x}Cu_xY_{10}$, reaching a maximum sample diameter of 7 mm at the $Mg_{65}Cu_{25}Y_{10}$ concentration [21]. It has recently been found that the GFA of Mg-Cu-Y BMGs can be improved by the partial substitution of Cu by transition metals, such as Ag [24], because of the large atomic size mismatch between Ag and the other constituents, the large negative heat of mixing in Ag-Mg and Ag-Y and the significant reduction in crystal growth rate [25]. At the same time, the thermal stability of these alloys slightly decreases with increasing Ag-content [25]. Recently Ma and co-workers have systematically monitored the variation of sample diameter in the three-dimensional composition space for the Mg-Cu-Ag-Y and Mg-Cu-Ag-Gd systems, showing the maximum value of 16 mm and 25 mm at $Mg_{54}Cu_{28}Ag_7Y_{11}$ and $Mg_{54}Cu_{26.5}Ag_{8.5}Gd_{11}$ concentrations, respectively [26]. As a consequence, Mg-based BMGs are excellent candidates to produce new light alloys for structural and functional applications with high applicability of near net shaping.

In the present paper, we demonstrate a comprehensive study on the GFA, thermal stability and crystallization kinetics of an amorphous Mg-Cu-Ag-Y bulk metallic glass. In addition, we present hydrogen desorption experiments on the fully amorphous and partially crystallized samples.

2. Experimental

2.1. Sample preparation

An alloy with a nominal composition of $Mg_{54}Cu_{28}Ag_7Y_{11}$ was characterized in the present study. Elemental pieces of Mg, Ag, Cu and Y (99.9 wt.% purity) were used as starting materials. As a first step, an intermediate binary Cu-Y alloy was prepared by induction melting in a Ti-gettered Ar atmosphere. Then this alloy was melted together with Mg and Ag in a water-cooled copper mould to obtain a master alloy. The master alloy was re-melted again for five times to ensure compositional homogeneity. As-cast cylinders with a diameter of 3 mm were obtained by injection of the molten liquid into a copper mould having a mass of two order of magnitude larger than the mass of the sample.

2.2. Characterization of microstructure

High resolution X-ray diffraction measurements applying monochromatic Cu Kα radiation were carried out on a double crystal diffractometer with negligible instrumental broadening. The diffractometer was equipped with a fine focus rotating copper anode (Nonius, FR 591) operating at 45 kV and 80 mA. The spot size of the X-ray beam on the specimen (100x300 μm^2) enables high spatial resolution. 2-dimensional diffraction patterns registered by FUJI Imaging Plate (BAS MS2025) were integrated after spatial distortion correction. Coherent

grain size of the partially or fully crystallized samples has been evaluated from the Scherrer formula [27]. Phase analysis has been carried out by the commercial PCPDFWIN software package.

Morphology studies of the as-cast alloy were carried out on a FEI QUANTA 3D dual beam scanning electron microscope (SEM) in back-scattered electron (BSE) mode on the surface of a 10x10 μm^2 notch sputtered by a focused ion-beam (FIB) setup operating at 30 kV with a current of 7 nA. Patterns were sputtered by a liquid gallium source. Local composition was quantitatively determined by energy dispersive X-ray (EDX) analysis with a relative accuracy of 1 %.

Some selected partially crystallized samples have been examined by transmission electron microscopy (TEM). The TEM lamellae were prepared from a piece of bulk material started by mechanical thinning down to 50 μm, followed by Ar-ion milling till perforation. The initial energy of the Ar-ions of 7 keV was finally reduced in 3 steps (3 keV and 1 keV) to 300 eV for removal of the surface layer caused by the ion bombardment and also remove surface oxide artifact. The samples were cooled by liquid nitrogen during ion milling to prevent transformation of the initial structure. The lamella was immediately inserted into the JEOL 3010 TEM (operated at 300 keV) to prevent formation of oxide artifact between preparation and examination. Images were recorded with a GATAN Imaging Filter (GIF Tridiem).

2.3. Thermal characterization

A power-compensated differential scanning calorimeter (Perkin Elmer DSC) was applied for continuous heating experiments at scan rates of 2.5 $Kmin^{-1}$, 5 $Kmin^{-1}$, 10 $Kmin^{-1}$, 20 $Kmin^{-1}$, 40 $Kmin^{-1}$ and 80 $Kmin^{-1}$. From the shift of the DSC peaks with increasing heating rate, the apparent activation energy of a transformation was determined [28]. The enthalpies of transformation were obtained as the area of the exothermic peaks. Isothermal annealing

experiments were carried out by heating the sample to the desired temperature at a rate of 100 $Kmin^{-1}$. The temperature and the enthalpy were calibrated by melting of pure Al and In. All measurements were carried out in Al sample pans under a protective flowing argon gas.

2.4. Hydrogen absorption measurements

High-pressure differential scanning calorimetry (HP-DSC) was applied on a SETARAM Sensys Evo TG-DSC equipment to investigate the hydrogen desorption during annealing of the as-cast and partially crystallized $Mg_{54}Cu_{28}Ag_7Y_{11}$ samples. The specimens were sealed in argon in a pressure cell and transferred to the HP-DSC apparatus. Then Ar was pumped out and the system was flushed by hydrogen (99.999%). Before each heating run, the hydrogen pressure was set to a constant pressure of 60 bar in order to achieve full hydrogenation. Subsequently, the hydrogen was pumped out from the apparatus and a linear heating scan at rate of 5 $Kmin^{-1}$ was applied in the 300 K - 470 K range.

3. Results

3.1. Continuous heating experiments

Continuous heating DSC curve obtained at a heating rate of 20 $Kmin^{-1}$ of the as cast $Mg_{54}Cu_{28}Ag_7Y_{11}$ alloy is presented in Fig. 1. A clear endothermic event corresponding to a glass-transition is followed by a supercooled liquid (SCL) region and two exothermic crystallization peaks (T_1,T_2). For further analysis of the thermal stability of the glass, additional representative temperatures, i.e the onset ($T_{g,on}$) and the end ($T_{g,end}$) of the glass transition and the onset of crystallization ($T_{x,on}$) were also determined by the intersect method, see the left inset in Fig.1. The width of the SCL range, defined as $\Delta T_x = T_{x,on} - T_{g,on}$, is usually used to estimate the stability of the liquid against crystallization. For the

$Mg_{54}Cu_{28}Ag_7Y_{11}$ system the ΔT_x = 49 K, in consistent with literature data [22]. The large value of ΔT_x is an indicative of the high resistance of the undercooled liquid to crystallization and consequently the nucleation of any primary crystalline phase is retarded. The right inset presents the melting enotherm of the alloy with the solidus (T_m=702 K) and liquidus (T_l=729 K) temperatures. The single sharp endothermic peak could refer to a eutectic concentration of the alloy, however, Ma et al. previously reported that the best BMG forming region in the Mg-Cu-Ag-Y system (around the $Mg_{54}Cu_{28}Ag_7Y_{11}$ concentration) is bit off-centered from the eutectic composition [26]. With the available data, additional GFA parameters, such as reduced glass transition temperature ($T_{rg} = T_{g,on}/T_l$) and γ parameter ($\gamma = T_{x,on}/ (T_{g,on}+T_l)$) can also be determined. The characteristic temperatures of the main transformations and the GFA parameters are listed in Table I. Both T_{rg} = 0.592 and γ = 0.414 refer to an excellent glass former [23,29]. At the glass transition, the thermogram exhibits the usual endothermic event (ΔH_g) which corresponds to a structural relaxation. The enthalpy of crystallization was obtained as the area of the first and second exothermic peak (ΔH_1 and ΔH_2). It is noted that Ag addition to Mg-Cu-Y alloys usually results in a more complex crystallization sequence instead of a single step transformation [29], in accordance with the wide SCL region.

The activation energy (E_a) and the frequency factor (Z) corresponding to glass transition and crystallization events can be determined from the Kissinger analysis [28]. For this purpose, additional continuous heating DSC runs were performed at different heating rates (β), ranging from 2.5 $Kmin^{-1}$ to 80 $Kmin^{-1}$ (Fig. 2). At all heating rates these curves present very similar behavior, however, higher heating rate results in higher characteristic temperatures (see Table I). The estimated average values of ΔH_g, = –16 Jg^{-1}, ΔH_1 = 47 $Jg^{-1}$and ΔH_2 =10 Jg^{-1} show little scatter with the heating rate. The dependence of peak temperatures on the heating rate can be given by the

$$\frac{\beta}{T_i^2} = \frac{Z_i R}{E_{a,i}} \exp\left(\frac{-E_{a,i}}{RT_i}\right) \quad (1)$$

equation, where R is the gas constant and the index i refers to g, 1or 2. The $\ln(\beta/T_i^2)$ vs. T_i^{-1} plot enables $E_{a,i}$ for each step from the slope of the fitted straight lines (see the inset in Fig. 2). The calculated values ($E_{a,g}$=161 kJmol^{-1}, $E_{a,1}$=107 kJmol^{-1} and $E_{a,2}$=104 kJmol^{-1}), in agreement with literature data [22], refer to high thermal stability and indicate that the crystallization takes place through a nucleation and growth mechanism. The frequency factor, which measures the probability that an atom with energy E_a joins to an existing nucleus, can be determined from the intercept of the fitted line with the ordinate. For the $Mg_{54}Cu_{28}Ag_7Y_{11}$ alloy the obtained values (Z_1=8*10^{22} s^{-1} and Z_2=3*10^{19} s^{-1}) are considerably lower than for Fe-based BMGs [30,31], indicating again the high GFA and resistance against crystallization. The deeper understanding of GFA of metallic glasses can be achieved through a correlation with fragility properties of the SCL [32]. Since glass transition is a kinetically modified thermodynamic phase transformation, $T_{g,on}$ varies with the heating rate. According to the Vogel-Fulcher-Tammann (VFT) approach, the variation of $T_{g,on}$ as a function of β can be ascribed as [33]

$$\beta = B \exp\left(\frac{A}{T_g^0 - T_{g,on}}\right),$$

or

$$T_{g,on} = T_g^{\,0} + \left(\frac{A}{\ln(B/\beta)}\right), \quad (2)$$

where A and B are constants and T_g^0 is the VFT temperature, usually approximated as the onset of the glass transition in the limit of infinitely slow cooling rate. The convincing fit of $T_{g,on}$ vs. β plot provides the VFT parameters, see Fig. 3. Undoubtedly, the data points deviate from a straight line, indicating a more VFT-like dependence of the calorimetric glass transition, rather than an Arhenius one [33]. Such non-linear behavior implies that the $Mg_{54}Cu_{28}Ag_7Y_{11}$ system exhibits an internal time scale of glass transition, which is proportional to the parameter B [33]. Noteworthy the large value of B (lnB = 6.35 K/s) indicates that a long waiting time is necessary to get the system achieving an ideal state. The inset of Fig. 3 shows the width of the glass transition, $\Delta T_g = T_{g,end} - T_{g,on}$ as a function of the logarithm of the heating rate. Evidently, ΔT_g obeys a clear linear behavior over the whole experimental range. As a remark, ΔT_g approaches zero at a critical heating rate ($\beta_{crit} = 1.2*10^{-3}$ $Kmin^{-1}$), below which the glass transition becomes independent of the time scale [33]. At this point $T_{g,on}$ also approaches T_g^0 since kinetic effects have no more effect on the glass transition. The fragility parameter (m) of the glass, which is equal to the steepness of the viscosity at the glass transition, can be given by the following equation [34]

$$m = \frac{A}{(1 - T_g^0 / T_{g,on})^2 T_{g,on} \ln 10}. \qquad (3)$$

The calculated fragility parameter is m=38 for the present composition, which in coincidence with that of $Mg_{59.5}Cu_{22.9}Ag_{6.6}Gd_{11}$ [32]. According to Angell's classification, such m value corresponds to an intermediate category of glass forming liquids, nevertheless it is much closer to the strong limit (m~16) than to the fragile limit (m>100) of metallic glasses [35]. Usually, the addition of Ag to Mg-based and Cu-Zr BMGs makes the SCL stronger resulting in the enhancement of GFA [32,36]. BMGs of low critical cooling rates exhibit relative small

fragility parameters in the range of 30–40 [34]. As was demonstrated by Battezzati et al. the reduced width of glass transition (ΔT_g /$T_{g,on}$) correlates with the inverse of the fragility parameter, i.e. $\Delta T_g/T_{g,on} = 2*m^{-1}$ [37]. Accordingly, the estimated values for the $Mg_{54}Cu_{28}Ag_7Y_{11}$ alloy is m=39, at a heating rate β=20 $Kmin^{-1}$, in line with the above kinetic approach.

The microstructural changes of the $Mg_{54}Cu_{28}Ag_7Y_{11}$ BMG associated with the linear heating experiments have been characterized by X-ray diffraction. Figure 4 presents the XRD patterns of the as-cast specimen, indicating broad and symmetric halos around 2Θ=38 deg and 2Θ=65 deg which is typical for a "X-ray amorphous" structure. The diffractogram corresponding to the first (lin 518K) transformation reveals the crystallization of several compound phases, i.e. orthorhombic Mg_2Cu (JCPDS 02-1315, a=0.527 nm, b=0.905 nm, c=1.821 nm), orthorhombic Cu_2Y (JCPDS 22-0255, a=0.431 nm, b=0.680 nm, c=0.732 nm), cubic MgY (JCPDS 18-0784, a=0.379 nm) and a possible minor traces of $AgMg_3$ (JCPDS 01-1170). The Bragg peaks of the crystalline phases are superimposed on a faint residual halo, indicating the amorphous component is still present at this stage. For the two major phases, the average crystallite size was about 17±2 nm. The final microstructure developed after the T_2 crystallization peak (lin 620K) consists of the similar Mg_2Cu, Cu_2Y, MgY and $AgMg_3$ phases with a complete vanish of the amorphous halo. At the same time, the Bragg-peaks become more intense and narrower corresponding to a mean crystallite size of 20±3 nm. In accordance with the results of Soubeyroux et al [29], the second thermal event includes only a moderate grain growth.

Figure 5 illustrates a typical SEM-FIB image taken from the inner surface of the ion-milled notch of the as-cast alloy. The composition of the matrix determined by the EDX analysis at several positions is equal to the nominal composition of the alloy within the experimental

error. The contrastless feature corresponds to a monolithic structure, no evidence of phase separation is observed.

3.2. Isothermal experiments

Isothermal annealing of the as-cast amorphous alloy was carried out at several temperatures (T_{iso}) in the range of 450 K-460 K in order to get a deeper understanding of the crystallization mechanisms. The T_{iso} values were selected slightly above $T_{g,on}$, but significantly lower than T_1, see the arrows in Fig. 1. The length of the isothermal annealings was selected on preliminary considerations [38]. As seen in Fig. 6, each isotherm exhibits a single exothermic peak, which practically incorporates the T_1 crystallization process obtained during the linear heating, as will be confirmed later. From the analysis of the shape of the isothermal DSC-peak it can be concluded that crystallization takes place through a nucleation from the amorphous matrix and a subsequent growth mechanism [39]. With increasing annealing temperature, the peak maximum (t_{iso}) occurs at shorter times (Table II). From the shift of t_{iso} as a function of T_{iso}, an apparent activation energy (E_{iso}= 110 kJmol^{-1}) was obtained. The enthalpy release during the various isothermal annelaings (ΔH_{iso}) slightly increases with T_{iso} (see Table II). The obtained value for ΔH_{iso} is approximately equal to ΔH_1, indicating that the during the isothermal heat release the first linear heating DSC-peak is eliminated.

The crystallization kinetics of the as-cast $Mg_{54}Cu_{28}Ag_7Y_{11}$ can be studied through the isothermal DSC experiments by applying the Johnson-Mehl-Avrami (JMA) model [40], as follows. The crystalline transformed fraction during the first thermal event (x(t)) at an instant T_{iso} temperature can be obtained directly from the isothermal curves according to the following equation

$$x(t) = \frac{\int_0^t \dot{H}(t')\,dt'}{\Delta H^{iso}} \quad , \tag{4}$$

where $\dot{H}(t)$ is the measured heat flow at time t. Figure 7a presents the x(t) isothermal transformation curves at T_{iso}=450 K, T_{iso}=455 K and T_{iso}=460 K on a logarithmic scale calculated from Eq 4. As it is evident, the reaction is completed in shorter times with increasing the annealing temperature. According to the JMA analysis, the x(t) transformed fraction can be written as

$$x(t) = 1 - \exp\left[-K(t-t_0)^n\right] , \tag{5}$$

where t_0 is an incubation time, n is the Avrami exponent describing the mechanism of the transformation and the kinetic factor K(T) follows an Arrhenius behavior

$$K(T) = K_0 \exp\left(-E_a/RT\right) , \tag{6}$$

where K_0 is a constant and E_a is the apparent activation energy of crystallization. The values of K and n can be determined from the

$$\ln[-\ln(1-x(t-t_0))] = n \ln K + n \ln(t-t_0) \tag{7}$$

equation. For single-step nucleation process, the $\ln[-\ln(1-x(t-t_0))]$ vs. $\ln(t-t_0)$ JMA plot is a straight line, and its slope and interception give n and K, respectively. Plots of this kind for the different T_{iso} temperatures are shown in Fig. 7b. As seen, a single exponent (n=3.8) is

necessary for T_{iso}=450 K to fit the JMA function, corresponding to a uniform nucleation mechanism. On the other hand, the JMA plots of T_{iso}=455 K and T_{iso}=460 K cannot be fitted with a straight line, even with varying t_0. In these cases more than one Avrami exponent is needed, because of the varying nucleation mechanism. The Avrami exponent can be written as

$$n= a +d*p, \quad (8)$$

where a is related to the nucleation rate, d represents the dimensionality of crystal growth and p refers to the mechanism that controls the growth [41]. The value 3.8 predicts interface-controlled 3-dimensional growth with decreasing nucleation rate.

An alternative experiment to get information on the crystallization mechanism under isothermal conditions is a linear heating scan following partial isothermal treatment for an instant time t_{ann}. Assuming that the total enthalpy release during the isothermal pre-anneal and the subsequent linear heating run is constant, the transformed volume fraction of the first crystallization event ($x(t_{ann})$) during the pre-anneal can be evaluated by obtaining the residual area of the first $\Delta H_1(t_{ann})$ crystallization reaction in the linear heating DSC experiments. Then the transformed volume fraction can be calculated as:

$$x(t_{ann}) = \frac{\Delta H_1 - \Delta H_1(t_{ann})}{\Delta H_1}. \quad (9)$$

Because of the single nucleation mechanism, T_{iso}=450 K temperature was chosen for this analysis, while the length of the pre-annealing treatment was selected as t_{ann} = 2500 s, t_{ann} = 4000 s, t_{ann} = 5000 s and t_{ann} = 7200 s, as indicated by arrows in Fig. 6. Figure 8 presents the

thermograms obtained during continuous heating corresponding to the different t_{ann} states. As evidenced, the area of the endothermic contribution ΔH_g diminishes progressively with increasing annealing time. At the same time the enthalpy release $\Delta H_1(t_{ann})$ also decreases monotonously, while $\Delta H_2(t_{ann})$ remains practically constant (see Table III). It is also noted that the second crystallization step splits into two sub-peaks (ΔH_2 and ΔH_{2*}) at longer annealing times, corresponding to a potentially different chemical composition of the residual amorphous matrix. The calculated values of $x(t_{ann})$ plotted in Fig. 7a fit satisfactorily to the transformation curve obtained from isothermal measurement, indicating that both procedures are valid for determining the transformed crystalline fraction. The variation of $T_{g,on}$,T_1 and T_2 as a function of t_{ann} can be seen in Fig 9. Each characteristic temperature obeys a gradual decrease, which reflects to decreasing thermal stability and a compositional change of the residual amorphous matrix.

The evolution of the crystalline phases during isothermal pre-anneals was also monitored by X-ray diffraction. The diffractograms obtained after annealing at T_{iso}=450 K for various t_{ann} times reveals the gradual reduction of the amorphous component (see Fig. 10). The first crystalline Bragg-peaks superimposed on the halo appear already after 2500 s of devitrification, a simultaneous precipitation of Mg_2Cu, Cu_2Y and MgY occurs. As the isothermal annealing prolongs, the crystalline peaks become more intense and sharper indicating a moderate grain growth (from 15 to 18 nm), in accordance with the calculated value of the JMA parameter. The presence of $AgMg_3$ is evident only after longer annealings. The X-ray diffractogram obtained after t_{ann}=7200 s exhibits similar phases to those found after linear heating at 20 $Kmin^{-1}$ up to 620K.

In order to reveal the details of the microstructure and morphology of the partially crystallized $Mg_{54}Cu_{28}Ag_7Y_{11}$ alloy, additional transmission electron microscopy were conducted on the sampler annealed at T_{iso}= 450 K for t_{ann} = 2500 s and t_{ann} = 7200 s. At first glance, a

remarkable difference cannot be resolved between the two bright field images, in both cases several nanocrystals exhibiting periodic atomic structure are homogenously dispersed in the aperiodic amorphous background (Fig. 11).

3.3. Hydrogen-sorption

Figure 12 presents the HP-DSC measurements of the reference $Mg_{54}Cu_{28}Ag_7Y_{11}$ fully amorphous BMG, partially crystallized states obtained either by continuous or isothermal annealing treatment and the fully crystallized alloy. The clear endothermic peak in the thermogram of the amorphous alloy (435 K – 465 K with a maximum at T_{des} = 451 K) can be assigned to the release of hydrogen. (It is noted that hydrogen absorption measurements were also carried out on all states, however, the effect is less characteristic, most probably due to baseline instabilities). As one can notice, this temperature range fairly well coincides with the SCL range of the alloy, namely the system remains in the glassy structure during the whole process of dehydrogenation. Complimentary XRD measurements has also been carried out on the fully amorphous alloy before linear heating, right after the hydrogen pressure was set to the constant pressure of 60 bar in the HP-DSC. Accordingly, it is stated that no crystalline hydride phase(s) formation is observed. A second diffractogram was also performed after the dehydrogenation in the HP-DSC device (after linear heating up to 470 K), confirming the presence only of the amorphous phase. The area of the endothermic peak corresponds to an enthalpy change of ΔH_{des}= –3.6 Jg^{-1}, which value proves the release of a hydrogen under the conditions of the HP-DSC. A repeating heating scan after a second hydrogenation exhibits the similar dehydrogenation behaviour, indicating that the H-uptake and release is an inherent reversible process of this glass, which do not frustrate of the as-cast atomic structure. A less-intense H-desorption peak (ΔH_{des}= –2.3 Jg^{-1}) at the same temperature characterizes the thermogram of the alloy treated isothermally at T_{iso} = 450 K for t_{ann} = 2500 s. A significant

drop in the temperature of desorption (T_{des} ~ 427 K) occurs after prolonged isothermal annealing (t_{ann} = 7200 s), which is associated with a remarkable decrease in the storage capacity (ΔH_{des}= –0.8 Jg^{-1}). Very similar features characterize the thermogram of the partially crystallized sample (T_{des} ~ 425 K, ΔH_{des}= –0.3 Jg^{-1}) treated by continuous heating above the first crystallization peak (lin 518 K). As also noticed, the fully crystallized sample (lin 620 K) possesses no detectable hydrogen sorption. As a comparison of the calorimetric and H-storage experiments, we can conclude that the decreasing amorphous content results in smaller hydrogen storage capacity and lower temperature of desorption.

4. Discussion

According to the "three dimensional pinpointing approach" of Ma et al. [26], it was found that the Mg-Cu-Ag-Y system exhibits extraordinary GFA in a rather wide composition region, with the best BMG-forming concentration located at $Mg_{54}Cu_{28}Ag_7Y_{11}$. Indeed, our comprehensive thermal characterization confirmed that this BMG shows excellent GFA parameters including $T_{g,on}$ = 432 K, ΔT_x = 49 K, T_{rg} = 0.592 and γ = 0.414.

It is well known that BMG formation is favored when the nucleation and growth of crystalline phases cannot compete with the glass formation. The enhancement of the GFA and the thermal stability of the SCL appear to correlate with the large atomic mismatch, electronic effects and negative heat of mixing between the constituents [19]. In our particular system the following atomic sizes are present: d_{Mg} = 0.16 nm, d_{Cu} = 0.128 nm, d_{Ag} = 0.144 nm and d_Y = 0.180 nm. As was shown, Ag addition to several good glass formers, such as Mg-Cu-Y [24], Mg-Cu-Gd-Y [23], Cu-Zr [36] broadens the supercooled liquid region, decrease the fragility and increases the resistance against crystallization. Silver optimizes the atomic packing because of volume mismatch and negative heat of mixing with the other constituents is larger than that of Cu, such as $E_{Ag\text{-}Mg}$ = –10 kJ/mol, $E_{Cu\text{-}Mg}$ = –3 kJ/mol $E_{Ag\text{-}Y}$ = –29 kJ/mol $E_{Cu\text{-}Y}$ = –

22 kJ/mol [24]. Consequently, the crystalline state is destabilized, in line with the low value of m. At the same time the activation energy decreases with Ag-addition [22], see also Fig. 2. Stronger metallic glass formers with smaller fragility (<40) are susceptible to strong chemical short range order (SRO), less free volume and increased amount of directional bonds [42]. Indeed, molecular dynamic simulations accompanied with X-ray absorption fine structure technique have demonstrated to formation of several local structural units in a MgCu(Ag)Gd alloy [43]. Moreover, the similar coordination numbers around each constituent both in the SCL region and in the equilibrium liquid state (above T_m) explain that this strong glass can be regarded as a "frozen" liquid [43].

In the following, let us discuss the correlation between observed H-storage properties and microstructure of the $Mg_{54}Cu_{28}Ag_7Y_{11}$ BMG. Based on Fig. 12, it is obtained that the fully amorphous glassy structure presents the highest storage capacity at a relatively low absorption temperature, compared to nanocrystalline Mg-based powders [4,5]. Although, H-storage capacity reduces both during continuous heating and isothermal annealing, the absorption temperature shifted towards lower temperatures in the case of partially crystalline samples, and this may be advantageous in terms of practical applications. At the same time, supplementary XRD and TEM analysis demonstrated that the microstructure (crystalline phases, average crystallite size) hardly varies with t_{ann} during isothermal annealing, or with the final temperature during continuous heating experiments (see Figs. 4, 10 and 11). The only exceptional difference between these states is the amount of the crystalline fraction, which is undoubtedly confirmed by the very similar H-absorption behavior and similar transformed volume fraction of the t_{ann} = 7200 s and lin 518 K states. (In both cases the T_1 devitrification stage is completed). Since several crystalline phases (Mg_2Cu, Cu_2Y, MgY and $AgMg_3$) nucleate simultaneously from the amorphous background, the average atomic displacement during this process is relatively short and comparable to the crystallite size (~10

nm). At the same time average concentration of the residual matrix slightly changes, however, calorimetric experiments exhibit significant differences due to even minor changes of BMG concentration, as Fig. 8 also reveals. Consequently, the effect of chemical heterogeneities on length-scale larger than a couple of 10 nm is negligible at any heat-treated state. Note that during primary crystallization, the atomic diffusion length during crystallization can be remarkably higher accompanied with a drastic change in the matrix concentration. Based on the above experimental results, it is concluded that the hydrogen storage capacity practically correlates only with the crystalline volume fraction of the partially crystallized $Mg_{54}Cu_{28}Ag_7Y_{11}$ BMG and additional parameters, such as crystalline phase selection, crystallite size and change in the average matrix concentration do not play a significant role. However, molecular dynamic simulations revealed a significant difference in the SRO of the major crystalline phase (Mg_2Cu) and the glassy structure in MgCu(Ag)Gd BMG [43]. In the crystalline phase the Mg-centered polyhedron is <0,0,12,3> while the Cu-centered cluster is <0,2,8,0> [43], where the integers in <..> denote the number of triangles, rectangles, pentathlons and hexagons, respectively, on the cluster surface. Notwithstanding, the SRO around the Mg atoms is significantly different (<0,2,8,2> and <0,3,6,4>) in the glassy state, which, on one hand suppresses the precipitation of the Mg_2Cu during cooling the liquid below the glass transition and, on the other hand, can lead to an easier capture of hydrogen atoms. As it was evidenced from complimentary XRD analysis and HP-DSC scan, the fully crystallized alloy does not absorb hydrogen at all (see Fig. 12) even though MgY is among the nucleated phases, consequently it is reasonable to assume that the local atomic (glassy) structure in the supercooled liquid is accountant for the observed hydrogen sorption.

The connection between the glassy nature and the storage properties of the $Mg_{54}Cu_{28}Ag_7Y_{11}$ BMG is further supported by the mutual decrease in the glass transition temperature ($T_{g,on}$) and the H-sorption temperature (T_{des}) with increasing crystalline volume fraction (see Table

III and Figs. 8 and 12). Accordingly, the intrinsic structure of the amorphous phase plays a much more crucial role in the dehydrogenation than the presence or lack of any H-absorbing phase.

Conclusions

Comprehensive thermal characterization of as-cast $Mg_{54}Cu_{28}Ag_7Y_{11}$ bulk metallic glass revealed that this particular composition exhibits excellent glass forming ability, including $T_{g,on}$ = 49 K, ΔT_x = 49 K, T_{rg} = 0.592 and γ = 0.414. It was found that the calorimetric glass transition follows a Vogel-Fulcher-Tammann-like behavior. The calculated fragility parameter (m=38) corresponds to the intermediate category of glass forming liquids, close to the strong limit.

Both continuous heating and isothermal annealing experiments provoke the joint formation of several crystalline phases (Mg_2Cu, Cu_2Y, MgY, $AgMg_3$), which requires short atomic movements. Interestingly, the average size of these nanocrystals is practically unchanged during thermal treatment, only their volume fraction increases. According to the Johnson-Mehl-Avrami analysis the growth of the nanocrystals predicts 3-dimensional interface-controlled growth with decreasing nucleation rate.

Hydrogen-sorption experiments indicate that the as-cast fully amorphous alloy exhibits the largest enthalpy of desorption, compared to the partially and fully crystallized states. Since the fully crystallized alloy does not desorb hydrogen, it is assumed that the local atomic structure of the glass is accountant for the hydrogen release. The temperature of desorption fairly well coincides with the supercooled liquid range of the glass.

Acknowledgement

Á. R. is indebted for the János Bolyai Research Scholarship of the Hungarian Academy of Sciences. T.S. is grateful to the project UNION and FP7 project Beyond Everest. We acknowledge the support of the COST Action MP1103. The authors appreciate the support of G. Varga in the SEM experiments. Preparation of the TEM lamellae by N. Szász is acknowledged.

References

[1] Schlapbach L, Züttel A. Hydrogen-storage materials for mobile applications. Nature 2001;414:353-8.

[2] Varin RA, Czujko T, Wronski ZS. Nanomaterials for Solid State Hydrogen Storage. New York, NY, USA: Springer Science; 2009.

[3] Varin RA, Czujko T, Chiu Ch, Wronski Z. Particle size effects on the desorption properties of nanostructured magnesium dihydride (MgH_2) synthesized by controlled reactive mechanical milling (CRMM). J Alloys Compd 2006;424:356-64.

[4] Zaluski L, Zaluska A, Tessier P, Ström-Olsen JO, Schulz R. Nanocrystalline Hydrogen Absorbing Alloys. Mater Science Forum 1996;225:853-8.

[5] Fátay D, Révész Á, Spassov T. Particle size and catalytic effect on the dehydriding of MgH_2. J Alloys Compds 2005;399:237-241.

[6] Vittori Antisari M, Aurora A, Mirabile Gattia D, Montone A. On the nucleation step in the Mg-MgH_2 phase transformation. Scripta Mater 2009;61:1064-7.

[7] Oelerich W, Klassen T, Bormann R. Metal oxides as catalysts for improved hydrogen sorption in nanocrystalline Mg-based materials. J Alloys Compd 2001;315:237-42.

[8] Révész Á, Gajdics M, Spassov T. Microstructural evolution of ball-milled Mg-Ni powder during hydrogen sorption. Int J Hydrogen Energy 2013;38:8342-49.

[9] Zhang YH, Li BW, Ren HP, Guo SH, Wang XL. Hydrogenation and dehydrogenation behaviours of nanocrystalline $Mg_{20}Ni_{10-x}Cu_x$ (x = 0–4) alloys prepared by melt spinning. Int J Hydrogen Energy 2010;35:2040-7.

[10] Zhang YH, Zhao DL, Li BW, Ren HP, Guo SH, Wang XL. Electrochemical hydrogen storage characteristics of nanocrystalline $Mg_{20}Ni_{10-x}Cu_x$ (x = 0–4) alloys prepared by melt-spinning. J Alloys Compds 2010;491(1-2):589-94.

[11] Zhang YH, Li BW, Ren HP, Hu F, Zhang GF, Guo SH. Gaseous and electrochemical hydrogen storage kinetics of nanocrystalline Mg2Ni-type alloy prepared by rapid quenching. J Alloys Compds 2011;509:5604-10.

[12] Bendersky LA, Chiu C, Skripnyuk VM, Rabkin E. Effect of rapid solidification on hydrogen solubility in Mg-rich Mg-Ni alloys. Int J Hydrogen Energy 2011;36:5388-99.

[13] Kalinichenka S, Röntzsch L, Baehetz C, Kieback B, Hydrogen desorption kinetics of melt-spun and hydrogenated $Mg_{90}Ni_{10}$ and $Mg_{80}Ni_{10}Y_{10}$ using in situ synchrotron, X-ray diffraction and thermogravimetry. J Alloys Compds 2010;496:608-13.

[14] Denys RV, Poletaev AA, Maehlen JP, Solberg JK, Tarasov BP, Yartys VA. Nanostructured rapidly solidified $LaMg_{11}Ni$ alloy. II. In situ synchrotron X-ray diffraction studies of hydrogen absorption-desorption behaviours. Int J Hydrogen Energy 2012;37:5710-22.

[15] Spassov T, Köster U, Thermal stability and hydriding properties of nanocrystalline melt-spun $Mg_{63}Ni_{30}Y_7$ alloy. J Alloys Compds 1998;279:279-86.

[16] Révész Á, Kis-Tóth Á, Varga LK, Schafler E, Bakonyi I, Spassov T. Hydrogen storage of melt-spun amorphous $Mg_{65}Ni_{20}Cu_5Y_{10}$ alloy deformed by high-pressure torsion. Int J Hydrogen Energy 2012;37:5769-76.

[17] Teresiak A, Uhlemann M, Gebert A, Thomas J, Eckert J, Schultz L. Formation of nanostructured $LaMg_2Ni$ by rapid quenching and intensive milling and its hydrogen reactivity. J Alloys Compds 2009;481:144-51.

[18] Zhang QA, Jiang CJ, Liu DD. Comparative investigations on the hydrogenation characteristics and hydrogen storage kinetics of melt-spun $Mg_{10}NiR$ (R = La, Nd and Sm) alloys. Int J Hydrogen Energy 2012;37:10709-14.

[19] Inoue A. Stabilization of metallic supercooled liquid and bulk amorphous alloys. Acta Materialia 2000;48:279-306.

[20] Miller M, Liaw P: Editors. Bulk Metallic Glasses, An Overview. New York, NY, USA: Springer Science; 2009.

[21] Inoue A, Nakamura T, Nishiyama N, Masumoto T. Mg-Cu-Y bulk amorphous alloys with high tensile strength produced by a high-pressure die casting method. Materials Transactions JIM 1992;33:937-45.

[22] Hui X, Sun CY, Zhang CM, Liu SN, Wang ER, Wang ML, Chen GL. Mg–Cu–Y–Ag bulk metallic glasses with enhanced compressive strength and plasticity. J Alloys Compds 2010;504S:S6-9.

[23] Soubeyroux JL, Puech S, Blandin JJ. Effect of silver on the glass forming ability of MgCuGdY bulk metallic glasses. J Alloys Compds 2009;483:107-11.

[24] Park ES, Kang HG, Kim WT, Kim DH. The effect of Ag addition on the glass-forming ability of Mg–Cu–Y metallic glass alloys. J Non-Crystalline Solids 2001;279:154-60.

[25] Madge SV, Greer AL. Effect of Ag addition on the glass-forming ability and thermal stability of Mg-Cu-Y alloys. Mater Science Engineering A 2004;375-377:759-62.

[26] Ma H, Shi LL, Xu J, Li Y, Ma E. Discovering inch-diameter metallic glasses in three-dimensional composition space. Applied Phys Lett 2005;87:181915.

[27] Klug HP, Alexander LE, X-ray diffraction procedures for polycrystalline and amorphous materials. New York, NY, USA: Wiley; 1974.

[28] Kissinger HE. Reaction kinetics in differential thermal analysis. Analytical Chemistry 1957;29:1702-06.

[29] Soubeyroux JL, Puech S. Phases formation during heating of Mg–Cu–Ag–Y bulk metallic glasses J Alloys Compds 2010;495:330-3.

[30] Mitrovic N, Roth S, Eckert J. Kinetics of the glass-transition and crystallization process of $Fe_{72-x}Nb_xAl_5Ga_2P_{11}C_6B_4$ (x= 0, 2) metallic glasses. Applied Phys Lett 2001;78:2145-47.

[31] Révész Á. Crystallization kinetics and thermal stability of an amorphous $Fe_{77}C_5B_4Al_2GaP_9Si_2$ bulk metallic glass. J Thermal Anal Calorimetry 2008;91:879-84.

[32] Zheng Q, Xu J, Ma E. High glass-forming ability correlated with fragility of Mg–Cu (Ag)–Gd alloys. J Applied Phys 2007;102:113519.

[33] Brüning R, Samwer K. Glass transition on long time scales. Phys Rev B 1992;46:11318-22.

[34] Perera DN. Compilation of the fragility parameters for several glass-forming metallic alloys. J Phys: Condensed Mater 1999;11:3807-12.

[35] Angell CA. Formation of Glasses from Liquids and Biopolymers. Science 1995;267:1924-35.

[36] Song KK, Gargarella P, Pauly S, Ma GZ, Kühn U, Eckert J. Correlation between glass-forming ability, thermal stability, and crystallization kinetics of Cu-Zr-Ag metallic glasses J Applied Phys 2012;112:063503.

[37] Battezzati L, Castellero A, Rizzi P. On the glass transition in metallic melts. J Non-Crystalline Solids 2007;353:3318-26.

[38] Révész Á, Lendvai J, Cziráki Á, Liebermann HH, Bakonyi I. Formation of nanocrystalline phases during thermal decomposition of amorphous Ni-P alloys by isothermal annealing. J Nanosci Nanotech 2001;1:191-200.

[39] Chen LC, Spaepen F. Calorimetric evidence for the micro-quasicrystalline structure of 'amorphous' Al/transition metal alloys. Nature 1988;336:366-8.

[40] Avrami M. Kinetics of phase change III. Granulation, phase change, and microstructure. J Chem. Phys 1941;9:177-184.

[41] Christian JW. The theory of transformations in metals and alloys, 2nd edition, Oxford, UK: Pergamon; 1975.

[42] Busch R, Bakke E, Johnson WL. Viscosity of the supercooled liquid and relaxation at the glass transition of the $Zr_{46.75}Ti_{8.25}Cu_{7.5}Ni_{10}Be_{27.5}$ bulk metallic glass forming alloy. Acta Mater 1998;46:4725-32.

[43] Wang XD, Lou HB, Wang SG, Xu J, Jiang JZ. Atomic packing in $Mg_{61}Cu_{28}Gd_{11}$ bulk metallic glass. Applied Phys Lett 2011;98:031901.

Figure captions

Figure 1. Continuous-heating DSC curve of the as-cast $Mg_{54}Cu_{28}Ag_7Y_{11}$ bulk metallic glass obtained at 20 $Kmin^{-1}$. The arrows indicate the temperature of annealing. Left inset is an enlarged part of the DSC trace showing how to determine the characteristic temperatures. Right inset presents the melting endotherm with the melting and liquidus temperatures.

Figure 2. Series of Continuous-heating DSC measurements of the as-cast $Mg_{54}Cu_{28}Ag_7Y_{11}$ BMG obtained at different heating rates. The inset shows the Kissinger plots corresponding to the glass transition and the two crystallization transformation.

Figure 3. Dependence of the onset of the glass transition on the logarithm of the heating rate. $T_{g,on}$ was fitted by Eq. 2. Inset shows the width of the glass transition on the logarithm of the heating rate.

Figure 4. X-ray diffraction patterns corresponding to the as-cast $Mg_{54}Cu_{28}Ag_7Y_{11}$ BMG and the states obtained by continuous heating.

Figure 5. Typical SEM-FIB images taken from the inner surface of the ion-milled notch corresponding to the amorphous $Mg_{54}Cu_{28}Ag_7Y_{11}$ alloy.

Figure 6. Isothermal DSC thermograms of the $Mg_{54}Cu_{28}Ag_7Y_{11}$ BMG. Arrows denote the length of pre-anneals.

Figure 7. (a) x(t) isothermal transformation curves corresponding to different annealing temperatures calculated from Eq 4 and (b) the corresponding JMA plots.

Figure 8. Continuous heating DSC curves obtained after partial annealing of the as-cast glass

Figure 9. Variation of the peak temperatures with the duration of pre-anneals.

Figure 10. X-ray diffraction patterns performed after pre-anneals of the $Mg_{54}Cu_{28}Ag_7Y_{11}$ BMG.

Figure 11. TEM images corresponding to pre-anneals of the as-cast glass at T_{iso} = 450 K for (a) t_{ann} =2500 s and (b) t_{ann} =7200 s. White contour lines indicate the precipitated nanocrystals

Figure 12. High-pressure DSC measurements on the as-cast, partially crystalline and fully crystalline $Mg_{54}Cu_{28}Ag_7Y_{11}$ alloy

Table captions

Table I. Characteristic parameters [onset ($T_{g,on}$) and the end ($T_{g,end}$) of the glass transition, onset of crystallization ($T_{x,on}$), width of the supercooled liquid region (ΔT_x), crystallization peaks (T_1,T_2) and transformation enthalpies ((ΔH_g, ΔH_1 and ΔH_2)] obtained from continuous heating DSC experiments at different heating rate (β) for the $Mg_{54}Cu_{28}Ag_7Y_{11}$bulk metallic glass. Solidus (T_m) and liquidus (T_l) temperatures obtained at heating rate of β=20 $Kmin^{-1}$ are also tabulated.

Table II. Maximum of the calorimetric peak temperature (t_{iso}) and enthalpy release (ΔH_{iso}) as a function of the isothermal annealing temperature (T_{iso}).

Table III. Variation of the characteristic thermodynamic parameters of continuous heating following partial isothermal treatment for different annealing times t_{ann}.

Table1

International Journal of Hydrogen Energy 39 (2014) 9230-9240

β ($Kmin^{-1}$)	$T_{g,on}$ (K)	$T_{g,end}$ (K)	$T_{1,on}$ (K)	ΔT_x (K)	T_1 (K)	T_2 (K)	T_m (K)	T_l (K)	ΔH_g (Jg^{-1})	ΔH_1 (Jg^{-1})	ΔH_2 (Jg^{-1})
2.5	424	442	464	40	476	523	--	--	-16,7	45	7
5	426	445	471	45	482	532	--	--	-15,7	46	7
10	428	449	475	47	488	541	--	--	-15,6	47	11
20	432	454	481	49	495	549	702	729	-14,7	49	10
40	436	460	489	53	501	556	--	--	-14,8	51	11
80	440	466	493	53	507	563	--	--	-16,0	47	9

Table I

Table2

International Journal of Hydrogen Energy 39 (2014) 9230-9240

T_{iso} (K)	t_{iso} (s)	ΔH_{iso} (J/g)
450	5374	35
455	2995	39
460	1388	42

Table II

Table3

International Journal of Hydrogen Energy 39 (2014) 9230-9240

	As-cast	2000 s	4000 s	5000 s	7200s
$T_{g,on}$ (K)	432	430	427	425	--
T_1 (K)	495	487	484	478	--
T_2 (K)	549	546	543	538	530
T_{2*} (K)	--	--	--	565	550
ΔH_g (J/g)	-14,7	-7,4	-5,5	-1,0	-0,4
ΔH_1 (J/g)	49	45	35	15	0
ΔH_2 (J/g)	10	10	11	11	11
ΔH_{2*} (J/g)	--	--	--	3	6

Table III

Figure1

Click here to download high resolution image

International Journal of Hydrogen Energy 39 (2014) 9230-9240

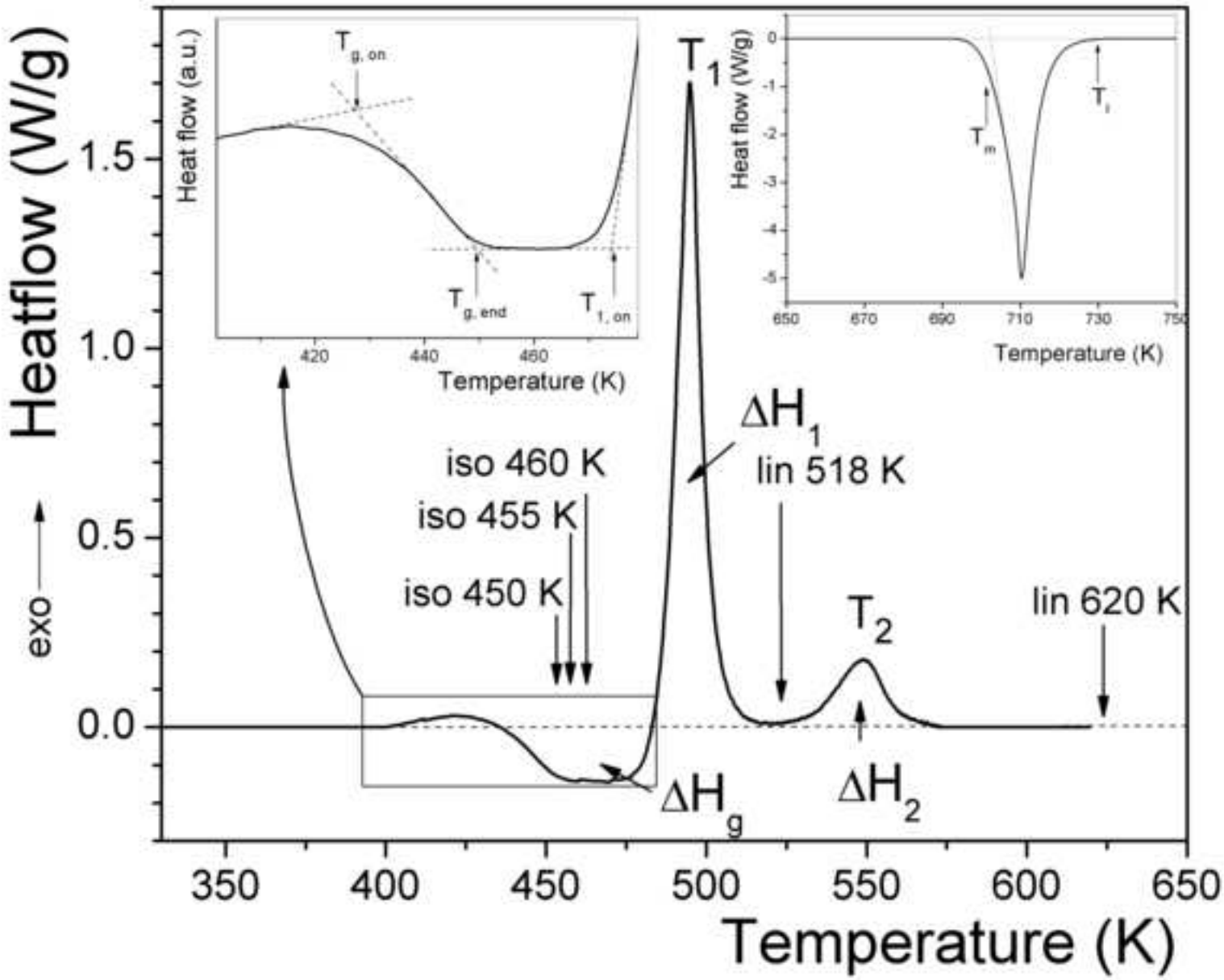

Figure2

Click here to download high resolution image

International Journal of Hydrogen Energy 39 (2014) 9230-9240

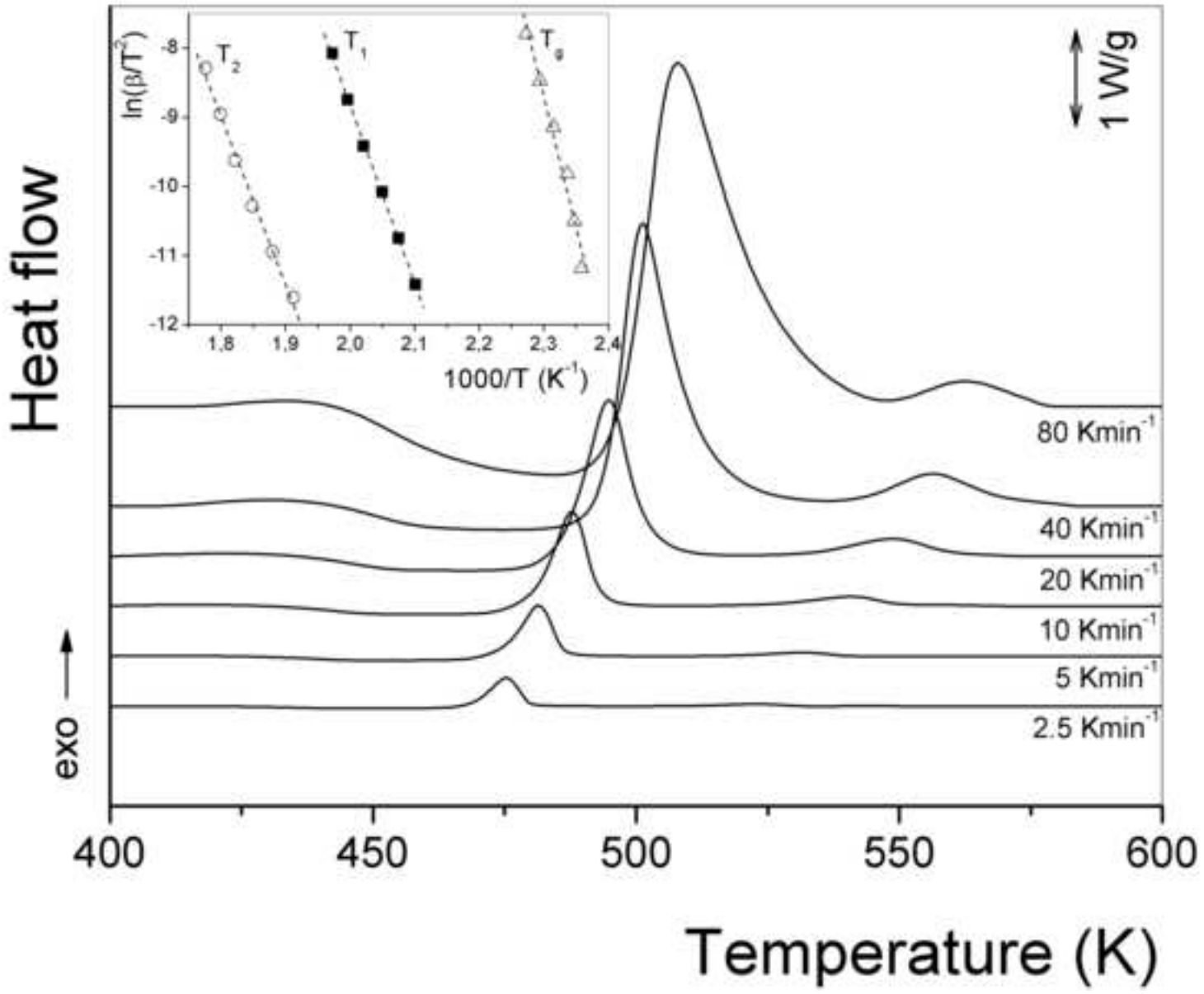

Figure3

Click here to download high resolution image

International Journal of Hydrogen Energy 39 (2014) 9230-9240

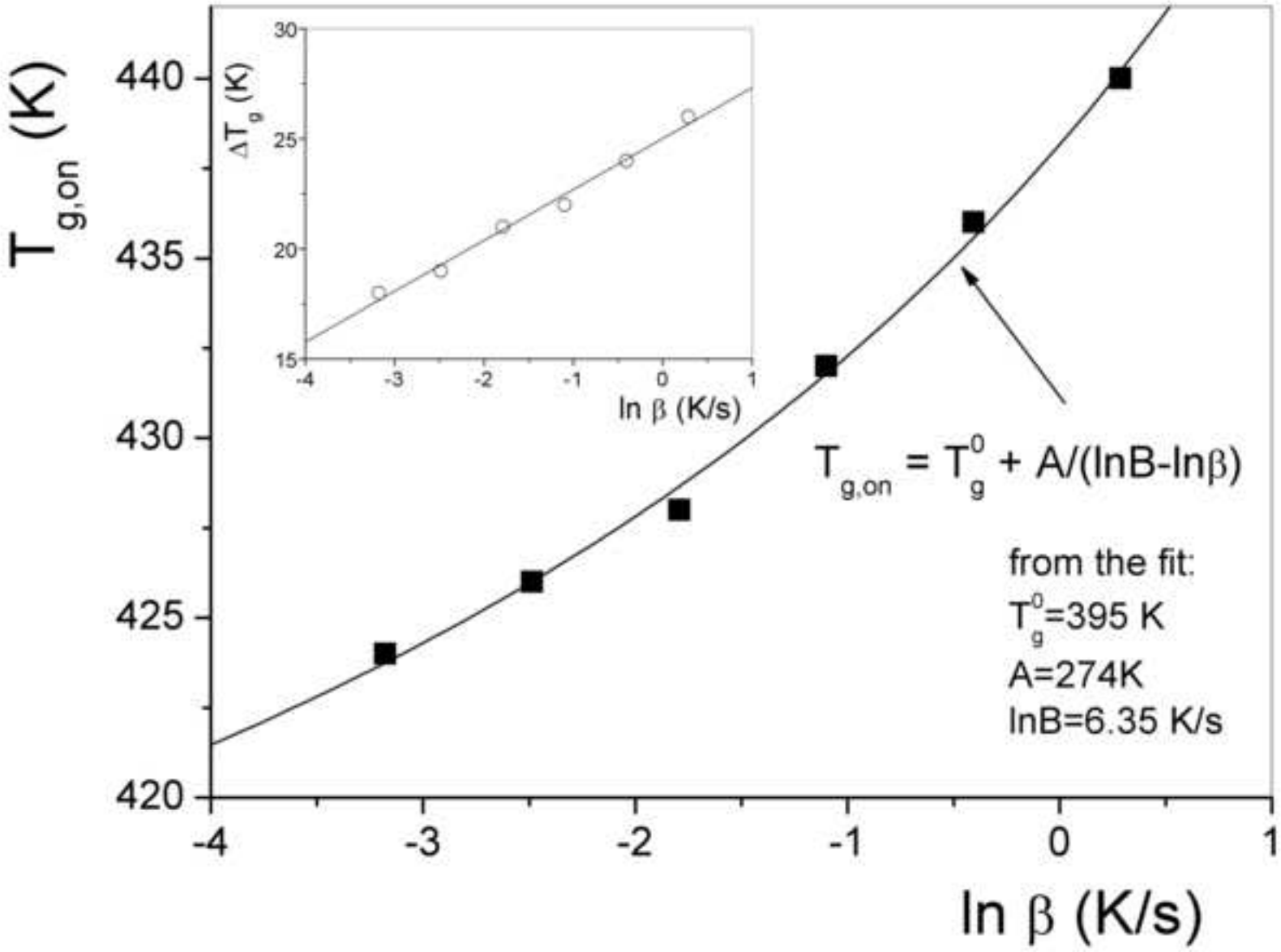

Figure4

Click here to download high resolution image

International Journal of Hydrogen Energy 39 (2014) 9230-9240

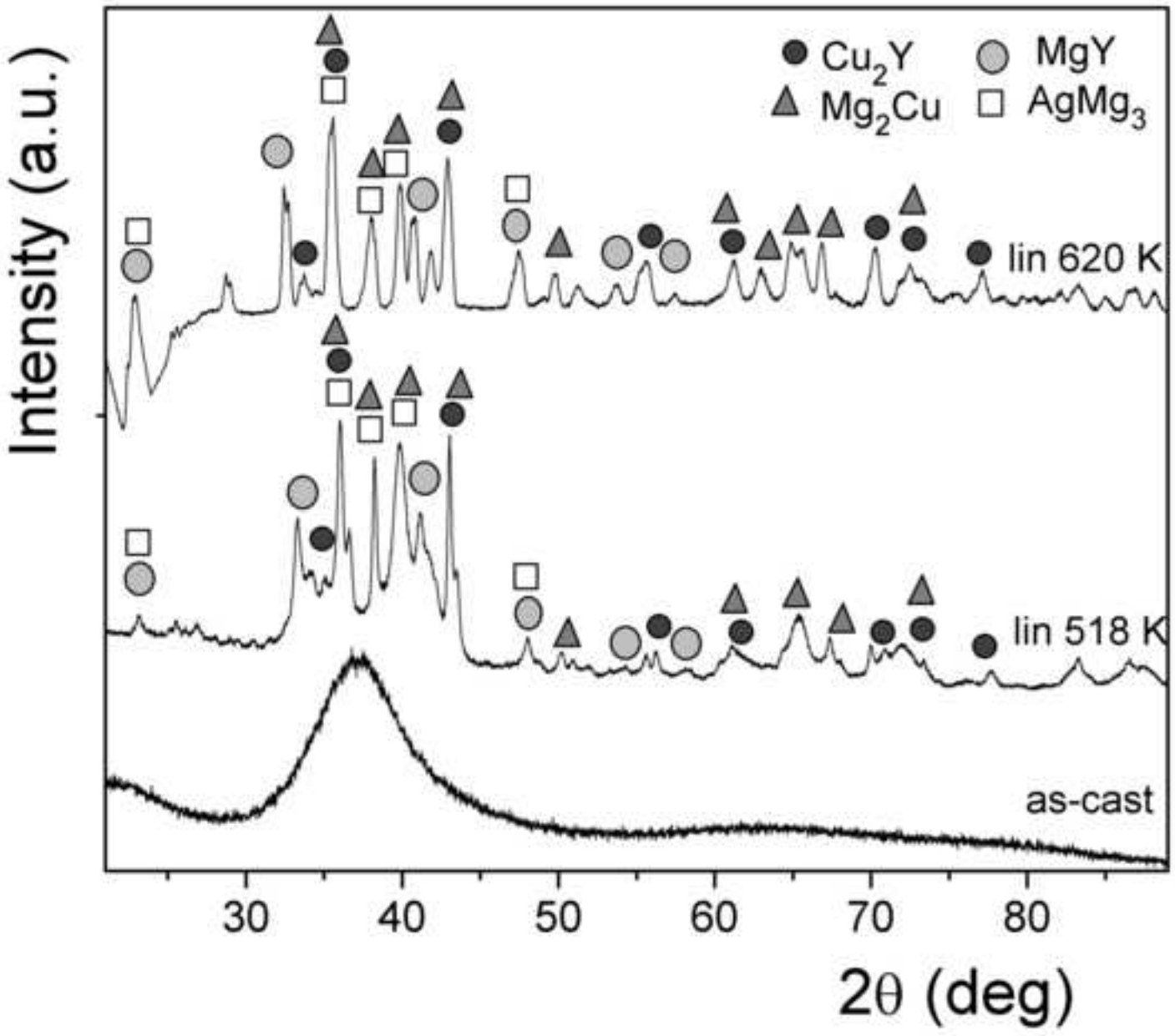

Figure5

Click here to download high resolution image

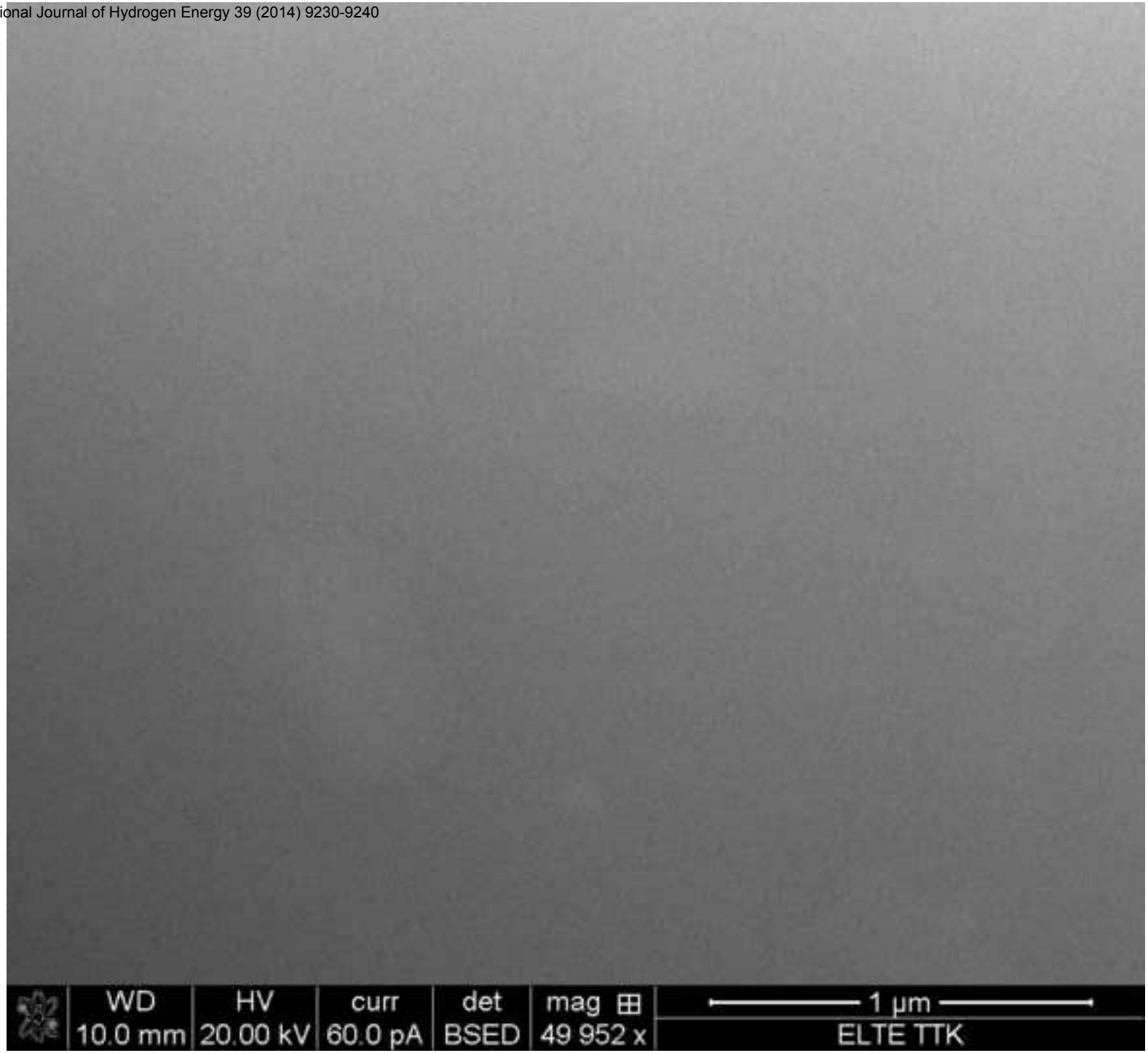

Figure6

Click here to download high resolution image

International Journal of Hydrogen Energy 39 (2014) 9230-9240

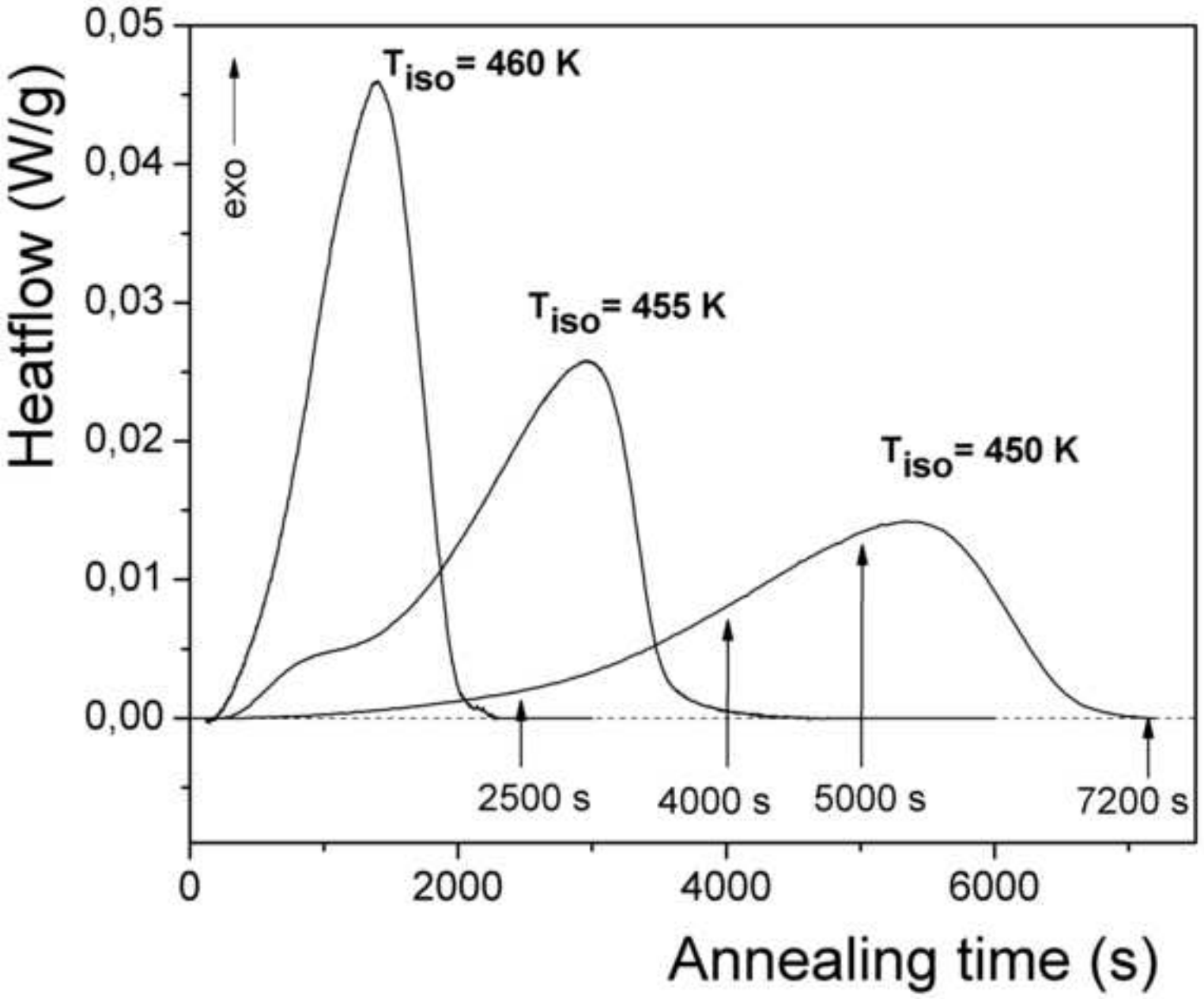

Figure7

Click here to download high resolution image

International Journal of Hydrogen Energy 39 (2014) 9230-9240

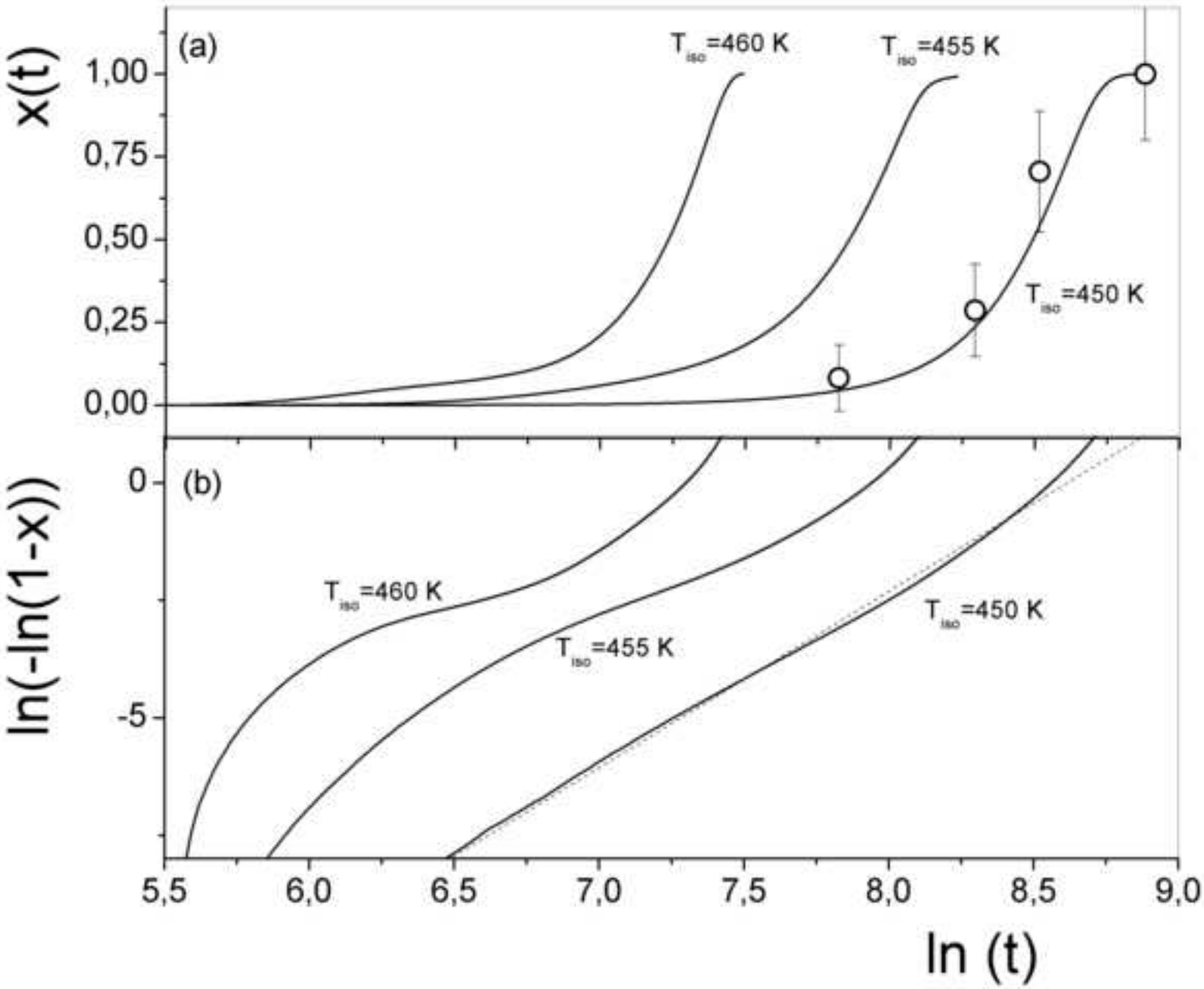

Figure8

Click here to download high resolution image

International Journal of Hydrogen Energy 39 (2014) 9230-9240

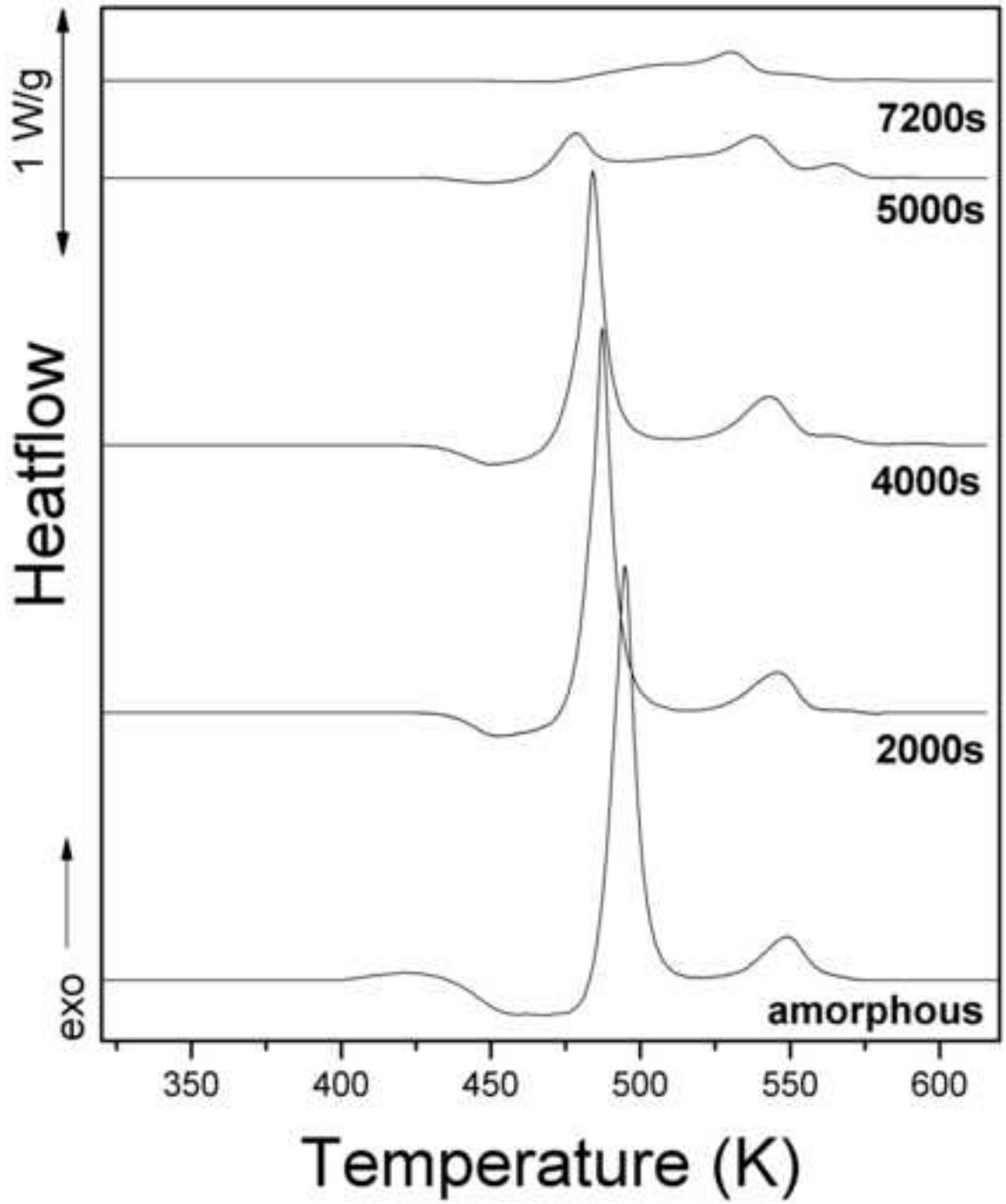

Figure9

Click here to download high resolution image

International Journal of Hydrogen Energy 39 (2014) 9230-9240

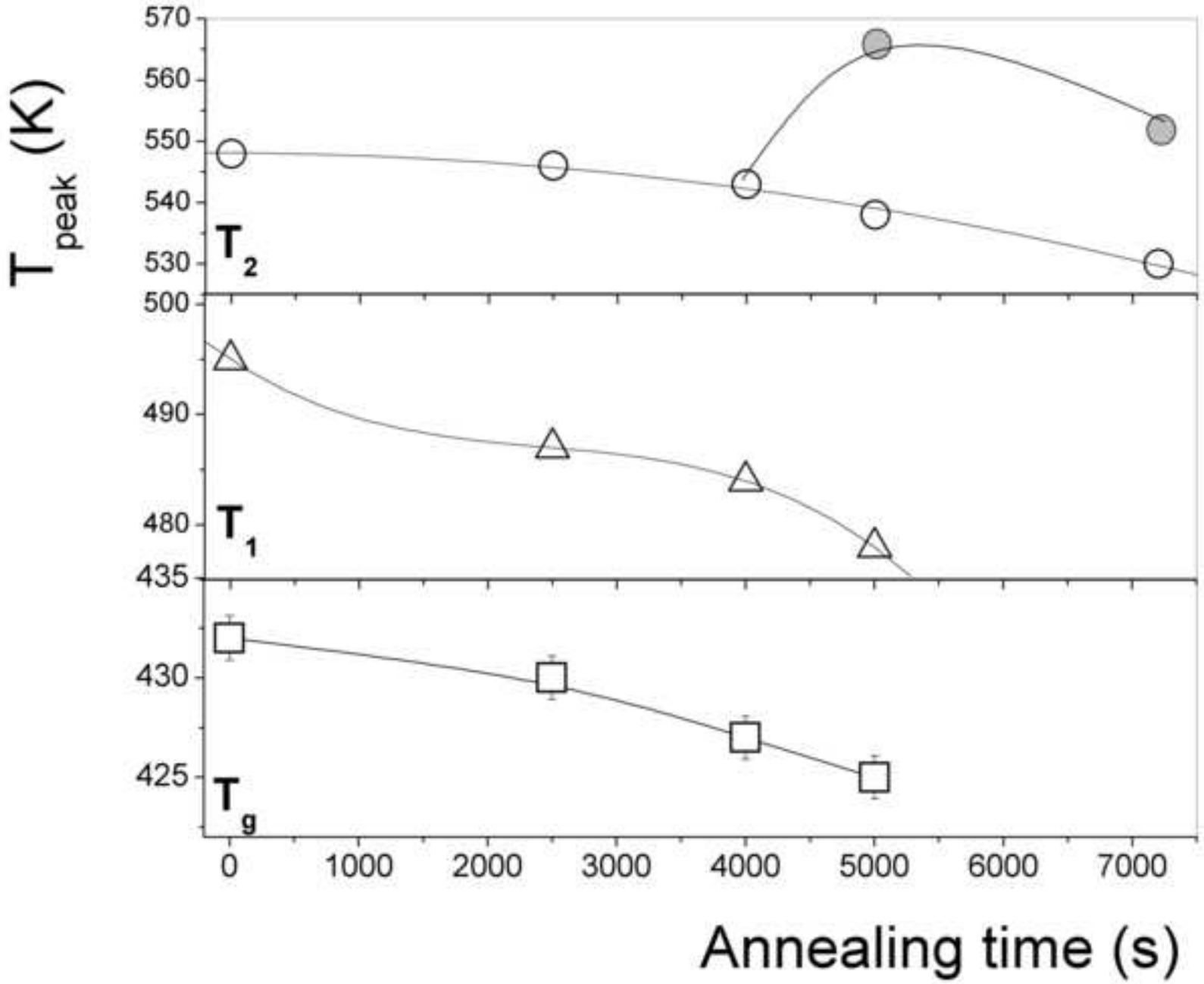

Figure10

Click here to download high resolution image

International Journal of Hydrogen Energy 39 (2014) 9230-9240

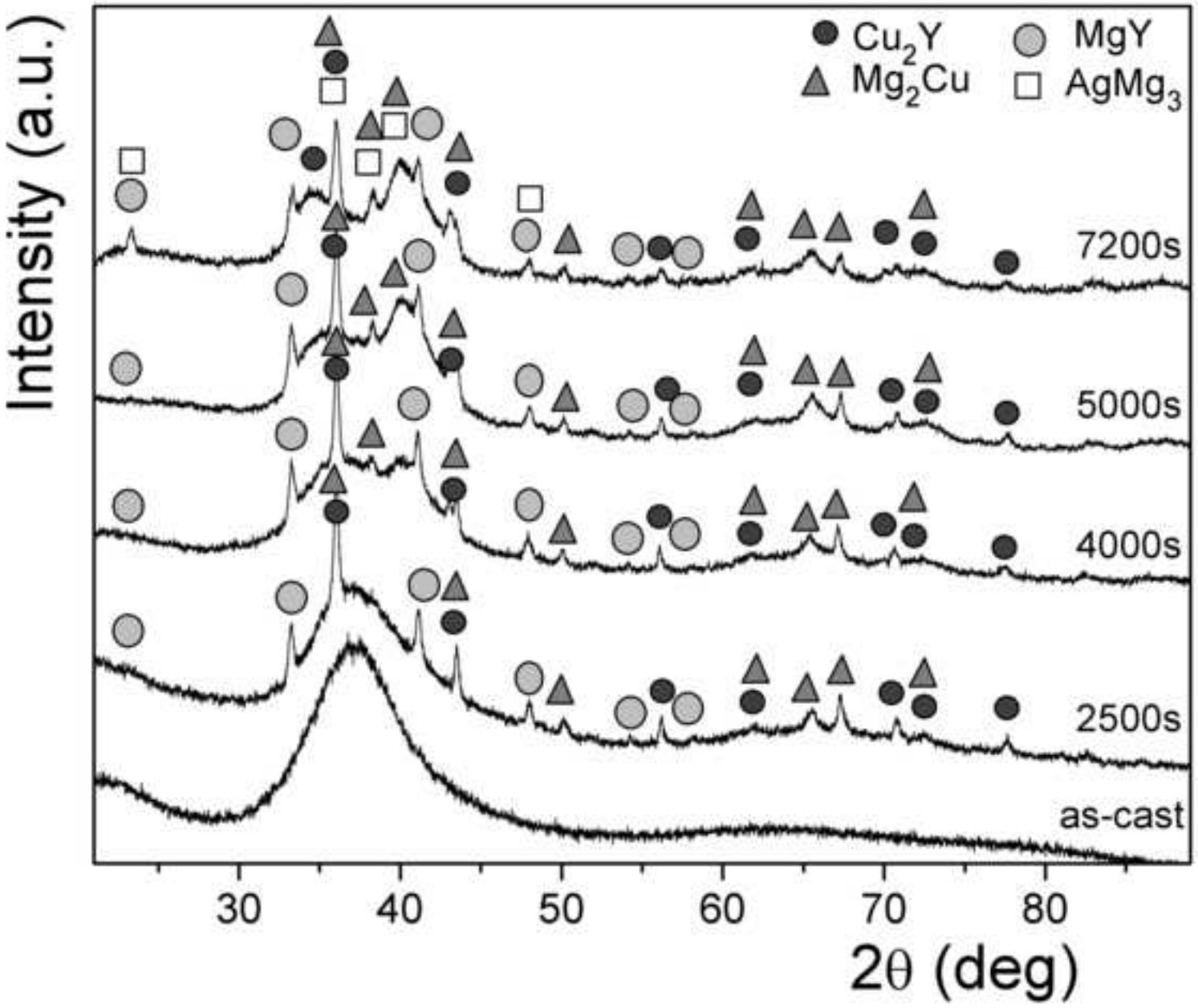

Figure11a

Click here to download high resolution image

International Journal of Hydrogen Energy 39 (2014) 9230-9240

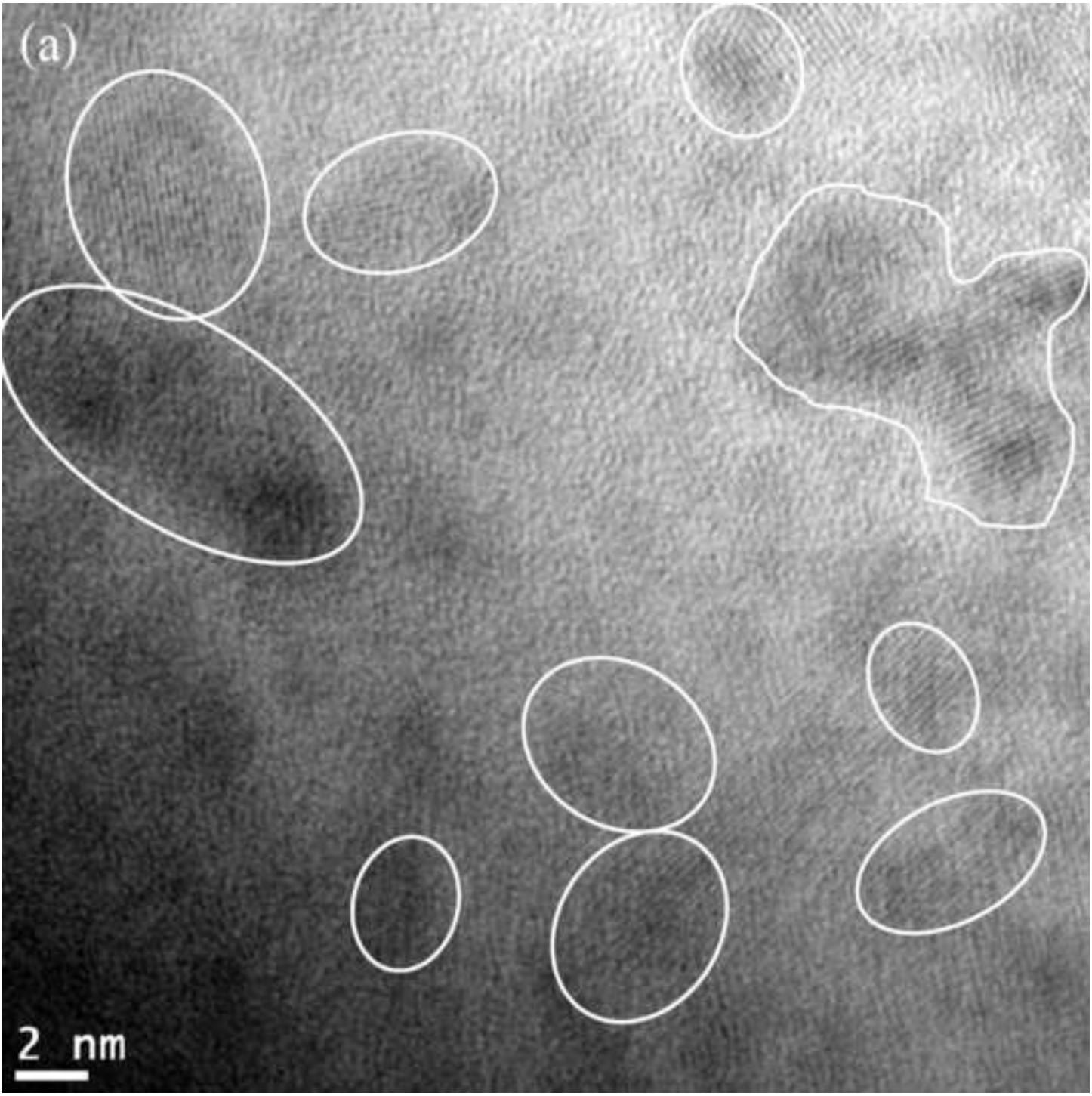

Figure11b

Click here to download high resolution image

International Journal of Hydrogen Energy 39 (2014) 9230-9240

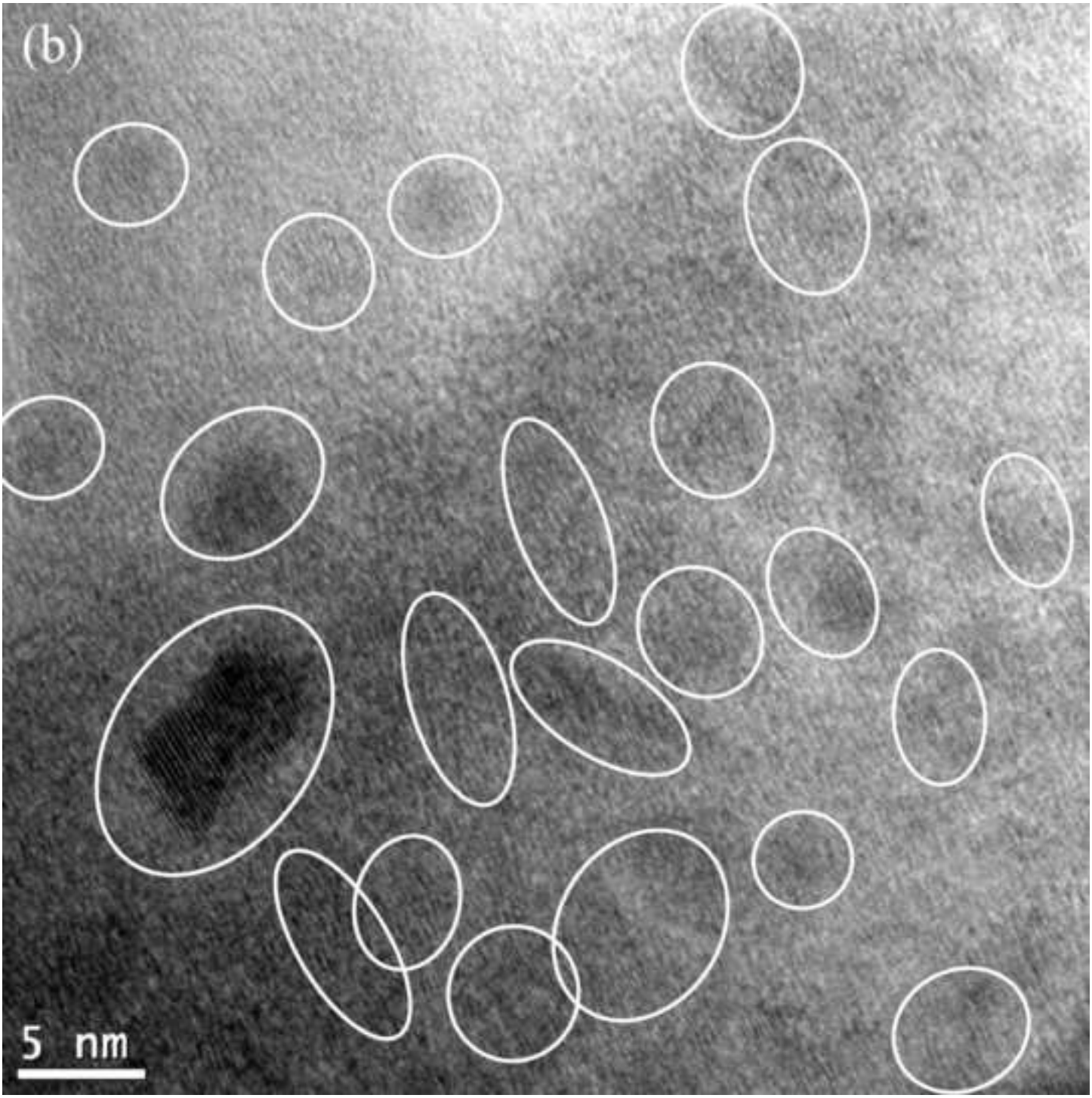

Figure12

Click here to download high resolution image

International Journal of Hydrogen Energy 39 (2014) 9230-9240